Polymer Crystallization Confined in One, Two, or Three Dimensions

Yueh-Lin Loo[†] **and Richard A. Register***

Department of Chemical Engineering and Princeton Materials Institute, Princeton University,
Princeton, New Jersey 08544-5263

Anthony J. Ryan

The Polymer Centre, Department of Chemistry, University of Sheffield,
Sheffield S3 7HF, United Kingdom

Gregory T. Dee

DuPont Central Research & Development, Wilmington, Delaware 19880-0356

Received August 24, 2001; Revised Manuscript Received October 1, 2001

ABSTRACT: We examine the crystallization behavior of polyethylene-*b*-poly(vinylcyclohexane) diblock copolymers, E/VCH, using a combination of transmission electron microscopy (TEM), dilatometry, and time-resolved small-angle X-ray scattering (SAXS). The glassy VCH matrix effectively restricts E crystallization to within the spheres, cylinders, gyroid channels, or lamellae formed by microphase separation in the melt. The VCH matrix can contract in response to crystallization of the E microdomains, so crystallization proceeds without cavitation. The crystallization kinetics strongly reflect the connectivity of the E microdomains: homogeneous nucleation and first-order crystallization kinetics for spheres or cylinders of E; conventional sigmoidal kinetics for the highly interconnected gyroid structure. Lamellar materials show an interesting two-step crystallization behavior: at higher temperature, heterogeneous nucleation permits the crystallization of lamellae interconnected through grain boundaries or defects, and then at lower temperature homogeneous nucleation permits the crystallization of the remaining isolated lamellae.

Introduction

The process of structure development in semicrystalline diblock copolymers, especially those having microphase-separated melts, is enriched by the presence of two competing self-organizing mechanisms.[1] Above the crystallization temperature, chemical incompatibility between the two blocks results in microphase separation; this process drives the system to form nanoscale spheres, cylinders, lamellae, or complex bicontinuous structures, depending on the relative block lengths. However, crystallization of one or the other block favors the formation of alternating crystalline and amorphous layers. Thus, the final solid-state structure adopted by a semicrystalline diblock depends on the interplay between microphase separation and crystallization.[2−5] In weakly segregated block copolymers, crystallization typically dictates the final solid-state structure, resulting in a lamellar morphology for any composition and often a spherulitic superstructure.[4−6] However, if the noncrystallizing majority block is vitreous during crystallization, the melt morphology can be faithfully reproduced in the solid state.[2,7−15] This is true even for weakly segregated systems since the presence of a glassy matrix forces crystallization to occur within the microdomains created by microphase separation. Lotz[10] pioneered the study of such semicrystalline−glassy block copolymers, working with poly(ethylene oxide)-*b*-polystyrene, EO/S—a system in which the crystal orientation with respect to the microdomain interfaces has only recently been elucidated.[11,12] Polymers whose crystallizable block is polyethylene (hydrogenated polybutadiene) have also been studied extensively. Cohen et al.[13] first demonstrated the preservation of spherical polyethylene microdomains following crystallization in a polyethylene-*b*-polystyrene diblock, E/S, whose S block glass transition temperature is above the E block freezing point. Hamley et al.[14,15] and Weimann et al.[8] subsequently demonstrated that spherical, cylindrical, lamellar, and gyroid melt morphologies were *all* retained upon crystallization in polyethylene-*b*-poly(vinylcyclohexane), E/VCH, di- and triblocks. Indeed, the glassy material need not be the mesophase matrix for the structure to be preserved: the hexagonal lattice formed by VCH cylinders in an E matrix is also preserved during E crystallization.[8,9]

Recently, we showed that confinement of E within spheres through strong interblock segregation resulted in first-order (exponential) crystallization kinetics and homogeneous nucleation.[2] These phenomena contrast starkly with the sigmoidal kinetics and heterogeneous nucleation ubiquitous in polymer crystallization. While the crystallization kinetics (e.g., Avrami exponent) and nucleation mechanism might be expected to show a strong dependence on the degree of crystal confinement imposed by the microdomain morphology, these effects have not been investigated across the range of morphologies which block copolymers exhibit. For E/VCH diblocks and VCH/E/VCH triblocks, Weimann[8] found that the temperature required to produce a specified level of crystallinity through a 1 h isothermal hold varied with morphology and noted a correlation with dimensional continuity of the E microdomains. Here, we employ this same E/VCH system to explore the effect that such confinement has on the crystallization kinetics and

---

[†] Present address: Bell Laboratories, Lucent Technologies, 600 Mountain Ave., Murray Hill, NJ 07974.

* To whom correspondence should be addressed: e-mail register@princeton.edu.

10.1021/ma011521p CCC: $20.00

Table 1. Characteristics of E/VCH Diblocks

sample	total M_n (kg/mol)	w_E	$w_{1,2}$ B block	E $T_{m,peak}$[a] (°C)	E $T_{c,onset}$[a] (°C)	w_c[b]	T_{ODT}[c] (°C)	melt structure
E/VCH 5/22	27.4	0.179	0.074	96	58	0.23	232	E spheres
E/VCH 6/25	30.8	0.180	0.072	96	63	0.31	>260	E cylinders
E/VCH 8/13	21.6	0.382	0.072	102	76	0.30	>260	E channels, gyroid
E/VCH 19/24	42.9	0.434	0.086	102	83	0.32	>260	E-poor lamellae
E/VCH 12/8	20.0	0.591	0.091	100	84	0.33	193	E-rich lamellae
E41	41	1	0.083	105	87	0.33		

[a] Measured by DSC at 10 °C/min. [b] Fractional crystallinity of E block; heat of fusion from DSC trace normalized by w_E and $\Delta H_m{}^0 = 277$ J/g. [c] Order−disorder transition temperature, measured via SAXS on heating.

nucleation mechanism. The kinetics, probed by time-resolved X-ray scattering, are found to be highly sensitive to microdomain connectivity, revealing (for example) the extent of interconnection between the microdomains in a lamellar specimen. The mode of crystal nucleation changes from heterogeneous to homogeneous[2] as the degree of connectivity between microdomains is reduced, but this is not a simple function of the volume fraction of crystallizable material. We also characterize the materials in real space by transmission electron microscopy, which can reveal the size, shape, and orientation of crystals within the microdomains.[16]

Experimental Section

Synthesis and Molecular Characterization. E/VCH diblocks were synthesized via sequential anionic polymerization of styrene (S) and butadiene (B) in cyclohexane at 60 °C followed by complete (>99%) catalytic saturation with $Pd^0/CaCO_3$, as described elsewhere.[9,16] The precursors to the E-poor sphere and cylinder formers were synthesized B block first and the others S block first. Only the precursor to E/VCH 19/24 showed detectable (ca. 1.5 wt %) terminated first block (S) by gel permeation chromatography (GPC), which was reduced below the detectability limit (<0.1 wt %) by fractionation in toluene/methanol prior to characterization and hydrogenation. GPC provided the molecular weight and polydispersity (always <1.1) of each diblock, via the molecular weight of the first block and the weight fraction of polystyrene as determined via ^{1}H NMR, which also revealed the fraction of 1,2-addition within the B block ($w_{1,2}$, uncertainty ± 0.005). Control of the 1,2 content is important because these units become ethyl branch defects in the E block upon saturation and affect both the melting point T_m and the degree of crystallinity; $dT_m/dw_{1,2} \approx -2.9$ °C/% at $w_{1,2} = 8\%$.[17,18] Molecular characteristics of the E/VCH diblocks, and a hydrogenated high-1,4-polybutadiene homopolymer prepared similarly (E41), are given in Table 1.

Transmission Electron Microscopy. As described in detail elsewhere,[16] slivers of E/VCH were stained by immersion in 0.5 wt % RuO_4 stabilized aqueous solution (Electron Microscopy Sciences). Absorption of Ru species provides the TEM contrast;[19] since diffusion of Ru is fastest through the noncrystalline portions of the E microdomains, amorphous E appears the darkest in all the micrographs. Because the extent of E domain connectivity differs greatly between the different morphologies, so did the immersion times: 9 days for sphere-forming diblocks, 4 days for cylinder formers, 24 h for the gyroid former, and 12 h for the lamellar materials. For E/VCH 19/24, the lamellar microdomains were oriented prior to staining by flow alignment in a lubricated channel die[20] at 180 °C. The stained slivers were embedded in LR white medium-grade acrylic resin (Structure Probe), sectioned to ca. 60 nm with a diamond knife at room temperature and examined at 100 keV on a Zeiss 910 TEM.

Static Small-Angle X-ray Scattering. Static small-angle X-ray (SAXS) scattering profiles were collected using a compact Kratky camera (Anton-Paar) equipped with a position-sensitive detector (Braun OED-50M). The data were reduced using previously reported procedures[21] to obtain profiles of desmeared absolute intensity vs scattering vector, q, where $q = (4\pi/\lambda) \sin \theta$; λ is the radiation wavelength (Cu Kα), and 2θ is the scattering angle. We were able to determine, or in some cases place lower bounds upon, the order−disorder transition temperatures (T_{ODT}, see Table 1) of the E/VCH diblocks by monitoring the SAXS profiles as a function of temperature.[22]

Differential Scanning Calorimetry. The peak melting temperature, $T_{m,peak}$, and heat of melting, ΔH_m, of each diblock were obtained on heating at 10 °C/min after cooling at 10 °C/min from the melt, using a Perkin-Elmer DSC-7 equipped with an intracooler and calibrated with indium and tin. The E block fractional crystallinity w_c was calculated from ΔH_m:

$$w_c = \frac{\Delta H_m}{w_E \Delta H_m{}^0} \qquad (1)$$

where w_E is the E block weight fraction, and $\Delta H_m{}^0$ is the heat of fusion of 100% crystalline polyethylene[23] (277 J/g). The onset crystallization temperature ($T_{c,onset}$) of the E block of each sample was obtained on cooling at 10 °C/min. The glass transition temperatures (midpoints) of the VCH blocks in E/VCH 5/22 and 6/25 were both located at 135 °C on heating at 10 °C/min.

Pressure−Volume−Temperature (PVT) Experiments. PVT experiments on E/VCH diblocks were conducted using a Gnomix Research PVT apparatus.[24,25] The samples were first heated into the melt (180−210 °C) and then cooled to room temperature before each isobaric run. Runs were performed at 10, 60, and 120 MPa at nominal heating and cooling rates of 2.5 °C/min. As we were principally interested in the low-pressure behavior of these diblocks, only the 10 MPa data are presented here, but the 60 and 120 MPa data were not qualitatively different.

Time-Resolved Small- and Wide-Angle X-ray Scattering (SAXS/WAXS). Time-resolved simultaneous SAXS/WAXS measurements were conducted on beamline 8.2 at the Daresbury Laboratory, U.K., using an incident beam of $\lambda = 0.154$ nm as described in detail elsewhere.[26−28] The sample cell consisted of approximately 10−15 mg of polymer (annealed at elevated temperatures to ensure microdomain lattice order), sandwiched in an aluminum DSC pan (TA Instruments) with holes punched in both pan and lid and covered with 20 μm mica windows to prevent sample leakage. A Linkam DSC 600 hot stage (calibrated with indium) equipped with liquid nitrogen cooling was used for precise temperature control (±0.05 °C). SAXS data were collected with a Daresbury quadrant detector, and WAXS data were simultaneously collected using a curved INEL detector, each in 6 s time intervals (“frames”). Frame-by-frame transmittance was computed from ionization chambers ahead of and behind the specimen and used to subtract scattering from the empty cell (including the DSC pan and windows) from all SAXS data and to normalize for variations in incident beam intensity and transmission.

For isothermal crystallizations, samples were heated into the melt ($T_m < T < T_{ODT}$) and then quenched at 40−50 °C/min to a crystallization temperature (T_c) and held isothermally while we monitored crystallization through time-resolved SAXS/WAXS. Because of the fast cooling from the melt to T_c, a temperature gradient is set up across the sample, which requires some time to relax; we found[2,29] that the data are adequately represented by a 0.4 min time lag (after the probe temperature, outside the sample, reached T_c) prior to the

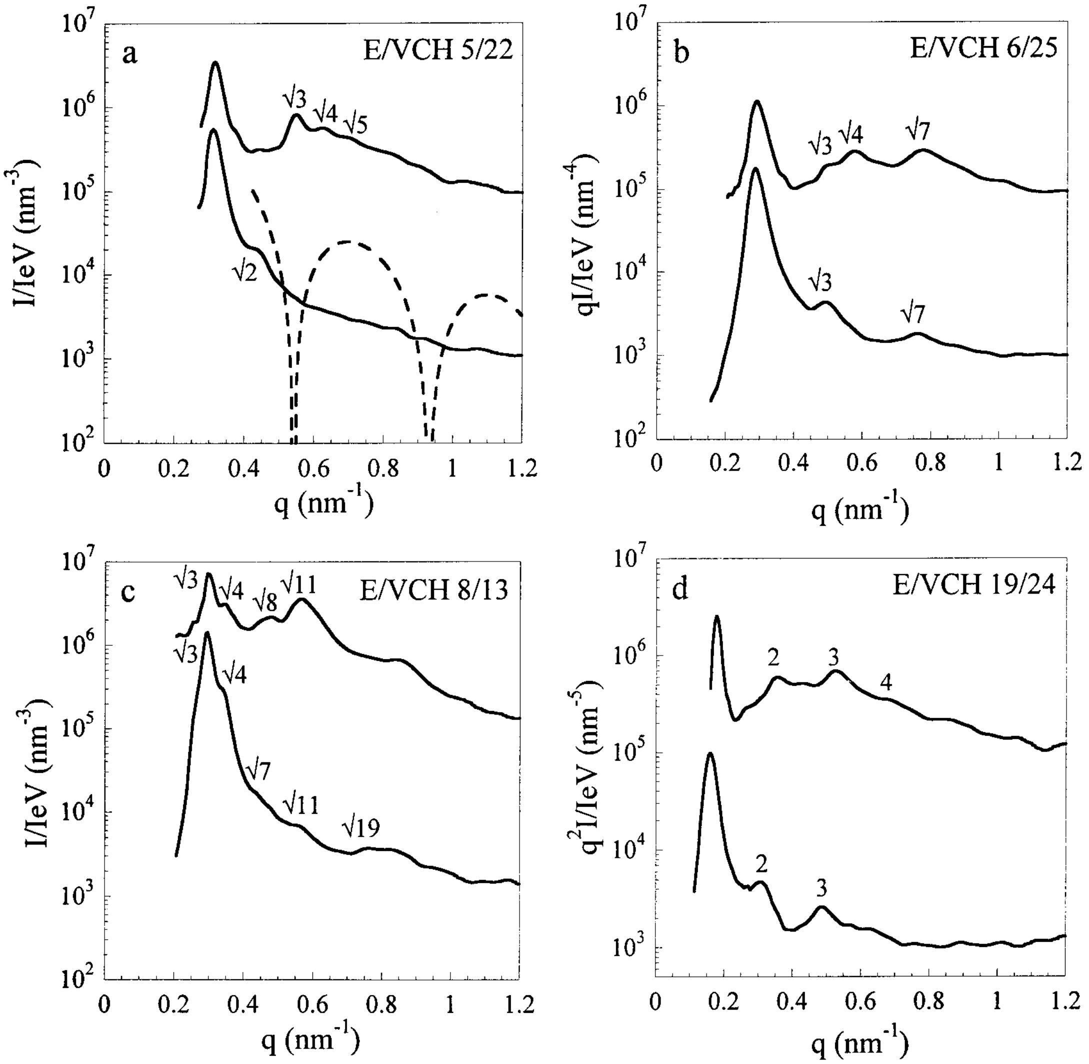

Figure 1. SAXS profiles taken in the melt at 160 °C (bottom profile in each panel) and at room temperature, after the samples had been fully crystallized (top profile in each panel): (a) sphere-forming E/VCH 5/22; (b) cylinder-forming E/VCH 6/25; (c) gyroid-forming E/VCH 8/13; and (d) lamellar E/VCH 19/24. The higher-order reflections associated with the respective structures are highlighted. In panel (a), the dashed curve is the calculated form factor for monodisperse E spheres of radius 8.3 nm.

isothermal hold, so $t = 0$ for all the plots shown was taken as 0.4 min after the probe temperature reached T_c.

Results and Discussion

Solid-State Characterization of E/VCH Diblocks. Figure 1 presents static SAXS patterns, in the melt at 160 °C and at room temperature, for each of four diblocks (one each forming an E-poor spherical, cylindrical, and gyroid structure, plus a lamellar diblock). In all cases, the principal features of the room temperature SAXS pattern—narrow primary peak at a position q^* essentially that of the melt, plus the presence of higher-order peaks—indicate that the melt morphology is faithfully preserved after crystallization, as expected. In all cases, the room temperature profiles contain enhanced scattering distributed over a broad range of q and peaked near 0.5–0.7 nm^{-1}. This additional scattering arises from the presence of small polyethylene crystallites within the E microdomains and is present in the hydrogenated polybutadiene E41 as well.[4,27,30]

In the melt, the E and VCH microdomains each have an essentially uniform electron density, with the electron density changing smoothly over the interfacial region. This regularity in electron density can lead to very small calculated intensities for some of the higher-order reflections which should be present given the symmetry of the lattice. In the case of the sphere-forming E/VCH 5/22 (Figure 1a), the $q/q^* = \sqrt{3}$ peak expected for a bcc lattice is visible only as a weak shoulder, because the form factor for scattering from spheres of the appropriate diameter (dashed curve in Figure 1a) has a minimum in this vicinity.[31] After E block crystallization, the electron density within the E domains is no longer uniform, nor is it precisely the same from one domain to the next; this can be seen directly in a published TEM image of E/VCH 5/22, which shows that each E microdomain contains one thin disklike crystal, randomly oriented.[16] Thus, the sharp form factor minimum indicated by the dashed curve in Figure 1a is no longer present, and higher-order peaks are easily seen, such as the $\sqrt{3}$ and $\sqrt{4}$ peaks for E/VCH 5/22. The effect is particularly striking for the gyroid-forming E/VCH 8/13, where the $\sqrt{11}$ peak increases dramatically in intensity upon crystallization (Figure 1c).

TEM micrographs of E/VCH 10/26, a cylinder-forming polymer similar to E/VCH 6/25, have also been published previously;[16] they show ribbonlike crystals of E running along the cylinder axis. Here, we turn to the

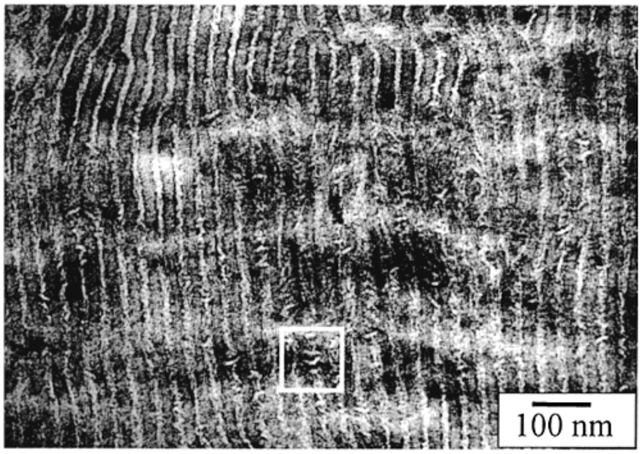

Figure 2. Transmission electron micrograph of fully crystallized E/VCH 19/24, oriented by channel die compression and stained with RuO_4. The box in the bottom center of the image highlights a region where lamellar crystals can be seen edge-on.

lamellar and gyroid cases. For E crystals which form within a lamellar structure, the *b*-axis (fast growth direction) is thought to lie in the plane of the E lamella, giving rise to short crystal lamellae whose stems lie parallel to the microdomain interface. This unusual orientation, deduced through X-ray analysis, was first found by Douzinas et al.[32] in polyethylene-*b*-poly(ethylethylene) diblocks and was studied in detail in E/VCH diblocks by Hamley et al.[14,15] Weimann et al.[8] presented a TEM image of a VCH/E/VCH triblock revealing heterogeneity within the E domains attributed to the crystallites, but the shapes and orientations of individual crystals were not resolved.

Figure 2 presents a TEM image for the lamellar E/VCH 19/24, with the section cut transverse to the lamellae, revealing unstained E crystals (white) sandwiched between glassy VCH sheets. In some areas (one highlighted by the white box), the crystals lie edge-on and appear as short stripes running roughly horizontally in the image, with an average crystal thickness of approximately 5 nm. Besides providing real-space confirmation for the structure presented by Douzinas[32] and by Hamley,[14,15] Figure 2 shows that there is a significant spread of crystal orientations with respect to the lamellar normal, even right at the interface. In many regions of the image, individual crystals are difficult to discern, presumably because they are oriented “flat-on” with respect to the electron beam. Even tilted crystals will be difficult to resolve in the image because they will overlap on projection through the section; only crystals with their thickness directions lying essentially in the plane of the section will appear edge-on in projection. The observation of a mixture of end-on and flat-on crystal orientations supports the idea of random orientation of the crystal stems in-plane.[14,15,32]

Figure 3 contains a TEM image of E/VCH 8/13, which forms the bicontinuous cubic gyroid phase. The image is a projection along the [100] direction,[33,34] as confirmed by the Fourier transform of the image (inset). However, individual crystallites within the E channels cannot be discerned. Observation of individual crystals would be thwarted if, as seems likely, the E crystals tend to follow the contours of the E channels rather than running straight through the section in an “edge-on” orientation.

PVT Experiments. While post-facto SAXS and TEM experiments revealed that the melt structure is preserved on crystallization in the E/VCH diblocks, i.e., crystallization occurs within the nanoscale domains prescribed by microphase separation, it remains unclear how the volume change due to crystallization of the dispersed phase is accommodated when the matrix is glassy. Consider the case of a sphere-forming diblock, such as E/VCH 5/22. One limiting case would be to assume that the matrix is perfectly rigid during crystallization. In this case, E crystallization would put each sphere’s contents under substantial hydrostatic tension. This tension could potentially be relieved through E domain cavitation, but either way, no change would be observed in the macroscopic specific volume vs temperature ($V-T$) curve at the E freezing point. A second limiting case would be to assume that the glassy matrix deforms affinely to accommodate the volume change due to crystallization. In this case, the macroscopic fractional change in volume ($\Delta V/V$) should be given by

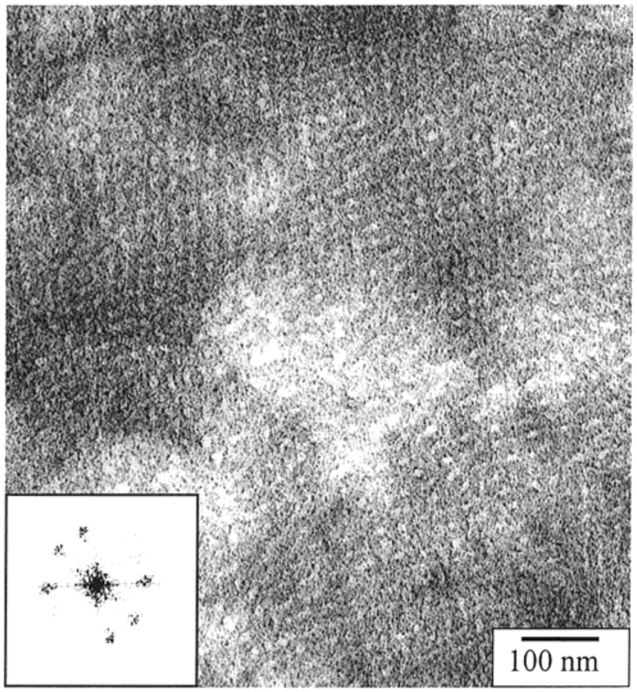

Figure 3. Transmission electron micrograph of fully crystallized, stained E/VCH 8/13. Inset shows the Fourier transform of the micrograph, characteristic of the [100] projection of the gyroid.

$$\frac{\Delta V}{V} = v_E w_c \left[\frac{V_{E,a} - V_{E,c}}{V_{E,a}}\right] \quad (2)$$

where $V_{E,a}$ and $V_{E,c}$ are the specific volumes of amorphous and crystalline polyethylene, v_E is the volume fraction of E in the diblock, and w_c is the weight fraction crystallinity of the E block. In amorphous block copolymers, thermal expansion mismatch creates a similar imbalance between inclusion and matrix; in B-poor S/B diblocks, Bates et al.[35] have presented evidence for both intact B microdomains under hydrostatic tension and cavitated B spheres, both examples of the first limiting case. For crystallizable materials, the only published dilatometric study appears to be that of Lotz and Kovacs[36] on a cylinder-forming S/EO diblock ($w_{EO} = 0.3$), which exhibited a macroscopic volume change upon crystallization generally consistent with eq 2, favoring the second limiting case.

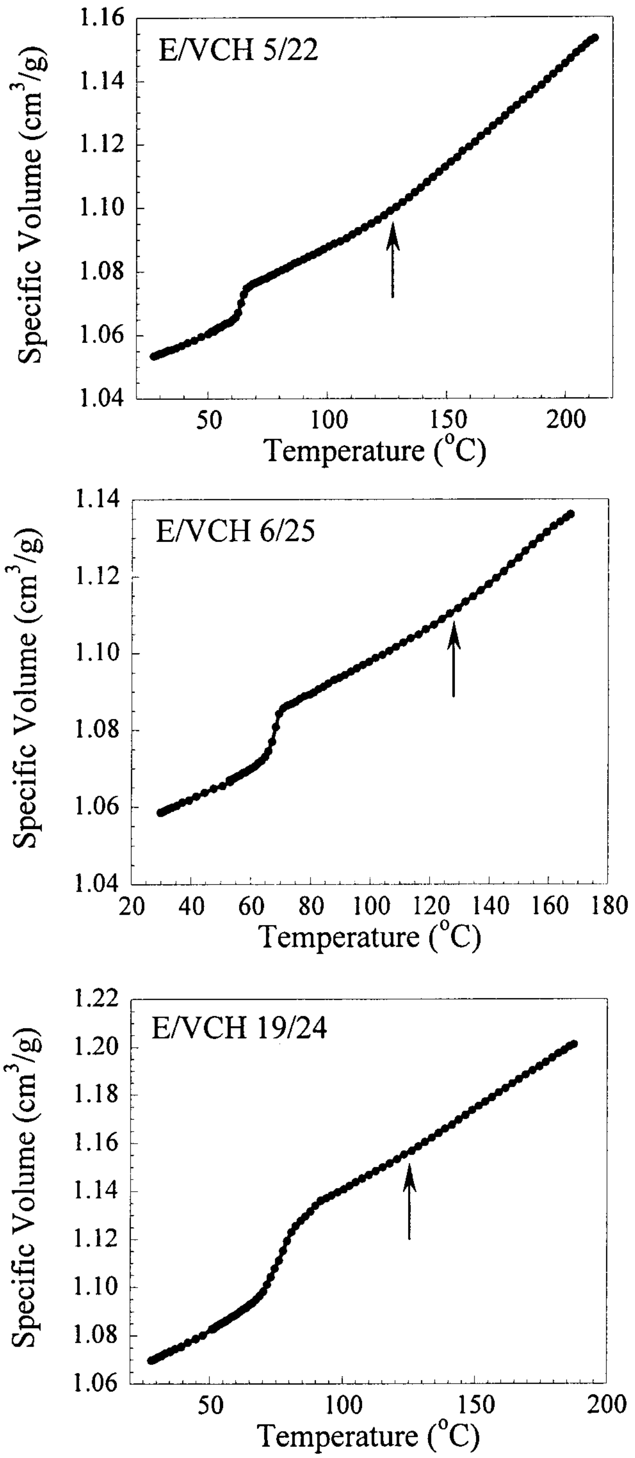

Figure 4. Volume−temperature data acquired on isobaric cooling at 10 MPa (nominal cooling rate 2.5 °C/min): (top) sphere-forming E/VCH 5/22; (middle) cylinder-forming E/VCH 6/25; (bottom) lamellar E/VCH 19/24. Arrows indicate the glass transition of the VCH matrix, while the step change at lower temperature is due to crystallization of the E domains.

We conducted specific volume measurements, on both cooling and heating, to compare our materials with these limiting cases over a range of microdomain morphologies. Figure 4 displays the $V-T$ curves for E/VCH 5/22 (spheres of E, top), E/VCH 6/25 (cylinders of E, middle), and E/VCH 19/24 (lamellae, bottom) acquired during isobaric cooling at 10 MPa. The change in slope in the vicinity of 130 °C reflects the glass transition of the VCH matrix, while the step change at lower temperature reflects the macroscopic volume change on crystallization. Table 2 lists the experimental values of $\Delta V/V$ alongside values calculated according to eq 2 using literature values of the necessary parameters;[37] w_c was estimated from DSC heating/cooling traces by integrating the endo/exotherm over the temperature interval where the volume change occurs and applying eq 1. The agreement is very good for all three diblocks on both heating and cooling, implying that even when the E blocks form spheres, the glassy VCH matrix can deform as necessary in response to E block crystallization. Indeed, for another cylinder-forming diblock (E/VCH 10/26), we had previously noted[16] that after crystallization the E cylinders exhibited slightly elliptical cross sections, with the lateral dimension of the ribbonlike crystal coinciding with the major axis of the ellipse—as if the crystal had "stretched" the microdomain perimeter into an ellipse. The ability of the VCH matrix to deform sufficiently without fracture may be aided by the short (<20 nm) distances between E microdomains, leading to a short "ligament thickness" for the PVCH.[38] The data of Figure 4 also rule out the possibility of substantial cavitation in these block copolymers, for any of the morphologies.

Table 2. Macroscopic Volume Changes Resulting from E Microdomain Crystallization and Melting

		crystallization, $\Delta V/V$ (%)		melting, $\Delta V/V$ (%)	
sample	morphology	measd	calcd	measd	calcd
E/VCH 5/22	spheres	0.7	0.7	1.0	0.8
E/VCH 6/25	cylinders	1.2	1.1	1.2	1.0
E/VCH 19/24	lamellae	2.2	2.8	2.8	2.4

One might expect that crystals confined to nanometer-scale microdomains would show a reduced melting point, due to an increased surface-to-volume ratio. However, inspection of Table 1 shows only a very small T_m depression; the sphere- and cylinder-forming diblocks melt approximately 5 °C lower than the lamellar diblocks. Confinement has only a small effect on the melting point in our polymers because the E crystals are intrinsically thin, with a thickness (ca. 5 nm) largely controlled by the ethyl branch content.[4,27,30] Thus, even when confined to microdomains 20 nm across, the vast majority of the crystal surface area is contributed by the surfaces perpendicular to the crystal stems, which are present even for unconfined crystals such as those in E41.

Kinetics and Mechanisms of Confined Crystallization. Figure 5 contains the SAXS profiles of E/VCH 5/22 acquired during isothermal crystallization at 62 °C, revealing how the SAXS pattern evolves between the melt- and solid-state patterns depicted in Figure 1a. The crystallization kinetics were quantified through the integrated (unweighted) SAXS primary peak intensity (which decreases upon crystallization, as the electron density difference between E and VCH diminishes), the SAXS intensity in q-intervals between macrolattice structure factor peaks (which increases as more crystals form; see Figure 1), and the intensity of the WAXS (110) reflection for orthorhombic polyethylene. All three quantities changed in parallel, but the small fraction of crystalline E present in these diblocks led to poorer statistical quality of the WAXS results, so results from the SAXS data are presented exclusively. The time (t) course of the integrated SAXS primary peak (E/VCH

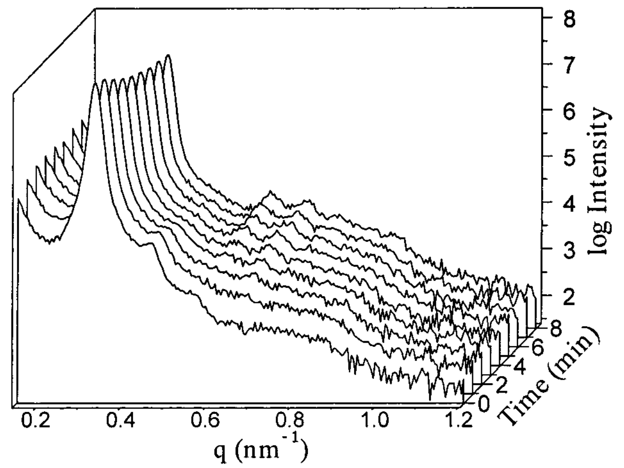

Figure 5. SAXS profiles taken during isothermal crystallization of E/VCH 5/22 at 62 °C. Time zero represents the time at which the sample first reached 62 °C. Each profile is accumulated over 1 min beginning at the time indicated.

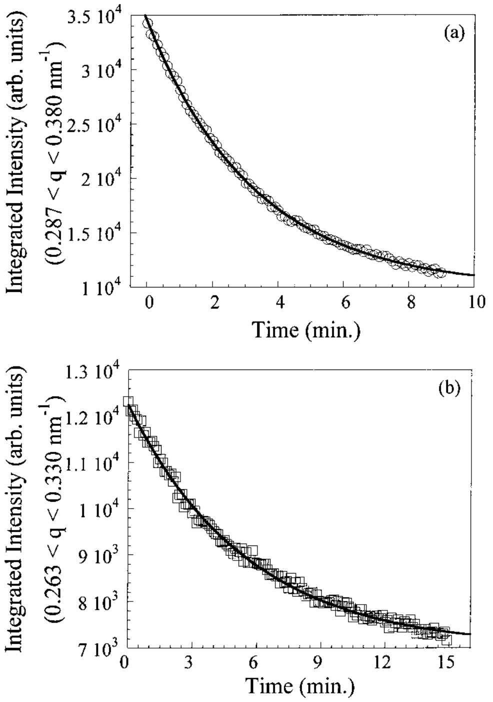

Figure 6. Time course of the integrated SAXS primary peak intensity during isothermal crystallization of (a) sphere-forming E/VCH 5/22 at 62 °C and (b) cylinder-forming E/VCH 6/25 at 66.5 °C. Both data sets are well described by an exponential decay (fits shown as continuous curves), yielding crystallization half-times of 2.2 and 3.8 min, respectively. Such first-order kinetics indicate that crystallization is isolated within individual microdomains.

5/22, 62 °C) is presented in Figure 6a. The data clearly follow first-order kinetics[2] and were fit as

$$1 - y = \exp(-kt) \tag{3}$$

where y is the fractional extent of transformation (with the crystallization halftime $t_{1/2}$ defined by $y = {}^1/_2$) and k the rate constant. Such first-order kinetics imply that crystallization is isolated within individual microdomains, resulting in a crystallization rate that is proportional to the fraction of material not yet crystallized.[2] Figure 6b contains the time course of the SAXS primary peak intensity for the cylinder-forming E/VCH

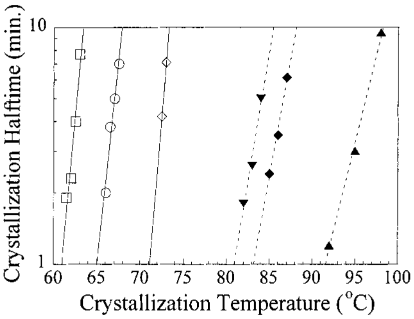

Figure 7. Crystallization half-times $t_{1/2}$ for the E/VCH diblocks and for E41. Open symbols represent systems that exhibit first-order crystallization kinetics, while filled symbols represent systems with sigmoidal kinetics. E/VCH 5/22 (□), E/VCH 6/25 (○), E/VCH 8/13 (▼), E/VCH 12/8, lower-temperature step (◇), E/VCH 12/8, higher-temperature step (◆), and E41 (▲).

6/25 acquired during isothermal crystallization at 66.5 °C. The crystallization process again proceeds via first-order kinetics, indicating that crystallization is effectively isolated within individual cylindrical microdomains in E/VCH 6/25.

If crystallization is truly isolated, the process must be individually initiated within each discrete microdomain, which can be achieved only through homogeneous nucleation.[2] Figure 7 contains a compilation of the crystallization half-time data as a function of isothermal crystallization temperature for all the diblocks; the slope of each curve is the temperature dependence (S) of the overall crystallization rate for that diblock. Typically S reflects a composite of the temperature dependences of both the nucleation and growth rates. However, crystal growth in E/VCH 5/22 and 6/25 is limited to the length of the microdomains (at most $O \sim \mu$m along the length of the cylinders), and E crystal growth at 60−70 °C is estimated to occur at $O \sim$ m/s,[39] so crystal growth within the spherical and cylindrical microdomains must be essentially instantaneous. Therefore, S in these samples reflects the temperature dependence of the nucleation rate alone.

The crystallization rates of both E/VCH 5/22 and E/VCH 6/25 have significantly steeper temperature dependences than that for the hydrogenated polybutadiene E41. Fitting the data of Figure 7 to exponential functions yields $S \approx 2.6$/°C and 2.2/°C for the sphere- and cylinder-forming diblocks (vs $S \approx 1.4$/°C for E41); i.e., for each 1 °C increase in the undercooling, the crystallization half-time increases by a factor of 2.6 in E/VCH 5/22 and 2.2 in E/VCH 6/25, and these factors directly reflect the change in the nucleation rate. These slopes are similar to that found previously for a sphere-forming E/SEB diblock[2] (2.9/°C) and are generally comparable to that for the homogeneous nucleation rate of linear polyethylene found by classical droplet experiments[40] ($S \approx 3.5$/°C at 85 °C), indicating that the individual microdomains within our semicrystalline diblocks are indeed homogeneously nucleated.

That homogeneous nucleation is responsible for initiating crystallization in E/VCH 5/22 and 6/25 is also clear from a simple calculation of the microdomain number density M; since isolated crystallization mandates one nucleus per microdomain, M must equal N, the number density of nuclei required to crystallize the entire sample. On the basis of the volume fraction of E and the volume of an individual sphere or cylinder[37] (assuming the cylinders extend for 1 μm, typical extent

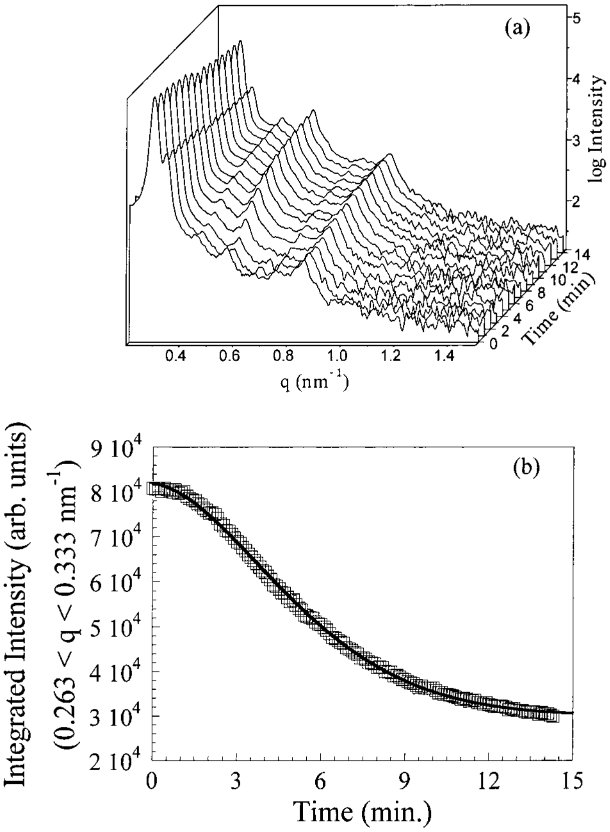

Figure 8. (a) SAXS profiles and (b) time course of the SAXS primary peak intensity during isothermal crystallization of the gyroid-forming E/VCH 8/13 at 84 °C. The data in panel (b) are well described by the Avrami equation (fit shown as continuous curve), yielding an Avrami exponent $n = 1.7$ and $t_{1/2} = 5.0$ min.

of a grain), $M_{\mathrm{E/VCH\ 5/22}} \approx 9 \times 10^{16}$ spheres/cm^3 and $M_{\mathrm{E/VCH\ 6/25}} \approx 2 \times 10^{15}$ cylinders/cm^3. These calculated values of M (and thus N) far exceed the heterogeneous nucleation density (due to impurities) typically found in hydrogenated polybutadienes ($N_i \approx 10^9$ impurities/cm^3 based on 10 μm diameter spherulites),[4] so the overwhelming majority of crystals must be homogeneously nucleated. The good correspondence between the nucleation rates here and in the sphere-forming E/SEB diblock studied previously[2] indicates an insensitivity to the identity of the matrix material (and thus to the local structure of the interface), consistent with true homogeneous nucleation.

By contrast, the gyroid-forming E/VCH 8/13 exhibits more conventional sigmoidal kinetics. Figure 8a shows SAXS profiles for E/VCH 8/13 during isothermal crystallization at 84 °C, while Figure 8b shows the time course of the integrated primary peak intensity. The data are well described by the Avrami equation:

$$1 - y = \exp(-kt^n) \tag{4}$$

with an Avrami exponent $n = 1.7$ and $t_{1/2} = 5.0$ min. The sigmoidal crystallization kinetics reflect the underlying connectivity of the E domains, which permits extended crystal growth along the E channels from a single nucleus. Though block copolymers typically show a polygrain structure, the grain boundaries are unlikely to be effective barriers to crystal growth in the gyroid structure, since only a small fraction of E channels in adjacent grains need to connect for crystals to grow from one grain to another. Thus, sigmoidal kinetics, rather than first-order, are expected and observed in the gyroid-forming diblock.

The shallower temperature dependence of the crystallization rate of E/VCH 8/13 ($S = 1.7$/°C) also suggests that the kinetics do not probe the rate of nucleation alone. The homogeneous nucleation rate for pure E at any temperature, $\dot{N}(T)$, may be estimated by extrapolating the data for E/VCH 5/22 in Figure 7, using its known sphere volume and E volume fraction, v_{E}. An estimate of the number of homogeneous nuclei generated during isothermal crystallization, N, may then be obtained as the product of the characteristic rate and time:

$$N = v_{\mathrm{E}}\dot{N}(T)t_{1/2} \tag{5}$$

With $\dot{N}(T) \approx 3 \times 10^9$ nuclei/(cm^3 min) for pure E at 84 °C, eq 5 yields an estimated density of 2×10^9 homogeneous nuclei/cm^3 generated upon isothermal crystallization at 84 °C in E/VCH 8/13. Unfortunately, since the calculated value of N is similar in magnitude to the typical density of active impurities within hydrogenated polybutadiene homopolymers ($\approx 10^9$ nuclei/cm^3), this comparison does not resolve whether homogeneous or heterogeneous nucleation dominates in this gyroid-forming diblock.

The substantial differences in crystallization kinetics between sphere- and cylinder-forming diblocks on one hand and the gyroid-forming diblock on the other indicate a strong dependence of the kinetics on the E domain connectivity, and lamellar samples provide a more interesting test of this idea. Consider a single perfect grain of lamellae, 1 μm or so in extent. Here, the lamellae are isolated from each other, and we would expect crystallization to proceed from homogeneous nucleation, with kinetics similar to those observed for E/VCH 5/22 and E/VCH 6/25. This picture is not significantly modified by the presence of dislocations ("extra" lamellae; examples can be seen near the top of Figure 2), which simply serve to connect two lamellae within a grain. But adjacent grains whose E lamellae connect across the grain boundary, or defects such as screw dislocations,[41,42] could lead to a high degree of connectivity between lamellae and crystallization kinetics akin to those observed for the gyroid structure.

Figure 9a displays the DSC trace for a lamellar diblock, E/VCH 12/8, acquired on cooling at 10 °C/min. Note the unusual double endotherm; the peak temperatures (75 and 64 °C) suggest two distinct populations of crystals, nucleated at different temperatures. It is tempting to ascribe the higher-temperature endotherm to a fraction of lamellae which are connected over a length scale of microns (such as across grain boundaries) and the lower-temperature endotherm to lamellae which are isolated. DSC traces for three different lamellar E/VCH diblocks showed an apparently random variation in the relative areas of these two endotherms; for E/VCH 19/24, the area fractions were approximately reversed from those shown in Figure 9a for E/VCH 12/8. Since particular defect and grain boundary structures are not imposed on the specimens, such variation is not unexpected; indeed, these observations suggest that crystallization kinetics may be a sensitive assessment of the degree of interconnection between lamellae.

To test this hypothesis, we conducted time-resolved SAXS/WAXS experiments during the crystallization of E/VCH 12/8, holding the specimen at temperatures which access the two crystallization processes sepa-

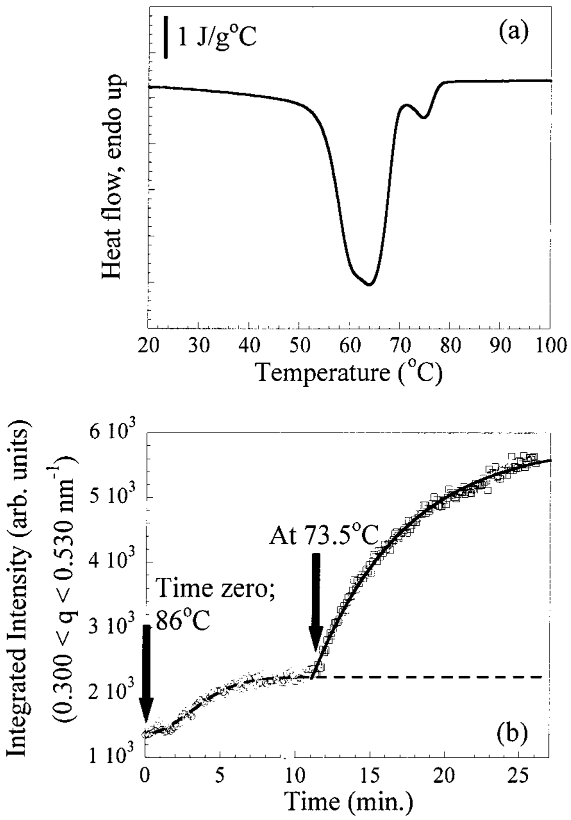

Figure 9. (a) DSC trace of lamellar E/VCH 12/8 on cooling at 10 °C/min. (b) Time evolution of scattering from crystallites (SAXS integrated between first- and second-order peaks) during two-step crystallization. Specimen was first held at 86 °C and quenched to 73.5 °C at the time indicated. Continuous curves represent fits via to the Avrami equation ($n = 2.0$, $t_{1/2} = 3.4$ min, first step of crystallization) and first-order kinetics ($t_{1/2} = 4.1$ min).

rately. The first-order SAXS peak in fully crystallized E/VCH 12/8 is rather weak, so to monitor the progress of crystallization, the SAXS intensity was integrated over a region between the first and second-order peaks of the lamellar structure, where changes in intensity reflect scattering from crystallites as they form. Figure 9b shows this integrated SAXS intensity as the sample is isothermally crystallized first at 86 °C (T_{c1}) and then at 73.5 °C (T_{c2}). During the isothermal hold at 86 °C, the time course of the integrated SAXS intensity is sigmoidal, with negligible crystallization occurring beyond 7 min. When the sample is quenched to 73.5 °C, crystallization resumes, but now following first-order kinetics. On the basis of the fits shown in Figure 9b, the first step of crystallization corresponds to 15% of the total, consistent with the areas of the two DSC endotherms shown in Figure 9a. If the two populations of crystals are defined by structural features such as grain boundaries, then we would expect the fraction of the crystallization process completed in the first step to be independent of T_{c1} and T_{c2}. While only a limited range of crystallization temperatures is practically accessible in the SAXS/WAXS experiment (corresponding roughly to $1 < t_{1/2} < 20$ min), we confirmed that the first step comprised 15 ± 1% of the total for T_{c1} ranging from 85 to 87 °C and T_{c2} ranging from 72.5 to 73.5 °C.

Following eq 5, the calculated density of homogeneous nuclei generated during the first step of crystallization in E/VCH 12/8 is only $N \approx 2 \times 10^7$ nuclei/cm^3, well below the typical density of heterogeneous nuclei. So in this first step, crystallization is heterogeneously nucleated, and crystal growth proceeds from one lamella to the next through defects or grain boundaries, allowing a single nucleus to generate crystals which pervade a three-dimensional volume much larger than an individual lamella. Such a process yields the sigmoidal kinetics observed, with a shallow temperature dependence of the crystallization rate (Figure 7, $S \approx 1.6$/°C) similar to that for E41. However, once the fraction of E lamellae that are connected to these heterogeneous nuclei are crystallized, no further crystallization occurs at 86 °C.

Table 3. Summary of Crystallization Behavior of E/VCH Diblocks

sample	melt morphology	Avrami exponent n	nucleation mechanism	S^a (/°C)
E/VCH 5/22	spheres	1	homogeneous	2.6
E/VCH 6/25	cylinders	1	homogeneous	2.2
E/VCH 8/13	gyroid	1.7	unclear	1.7
E/VCH 12/8^b	lamellae	2.0	heterogeneous	1.6
E/VCH 12/8^c	lamellae	1	homogeneous	2.9
E41		2.4	heterogeneous	1.4

[a] Temperature dependence of the overall crystallization rate, obtained from the data of Figure 7. [b] First step (higher temperature) in two-step crystallization process. [c] Second step (lower temperature) in two-step crystallization process.

The major fraction of E/VCH 12/8 is crystallized only when the sample is cooled to 73.5 °C, the second step of crystallization. The strong temperature dependence of the crystallization rate in this second step (Figure 7, $S \approx 2.9$/°C) and the calculated density of homogeneous nuclei generated during this second step ($N \approx 2 \times 10^{14}$ nuclei/cm^3 via eq 5) both indicate that the second step proceeds via homogeneous nucleation in the same way that crystals in the sphere- and cylinder-forming diblocks are nucleated. Figure 7 shows that the crystallization rate increases systematically on going from the sphere-forming E/VCH 5/22, to the cylinder-forming E/VCH 6/25, to the second step of the lamellar E/VCH 12/8. This is a direct consequence of the increase in individual microdomain volume on going from spheres to cylinders to lamellae; in each step of this progression, the volume increases by roughly 2 orders of magnitude, and since the nucleation rate *per E microdomain* is proportional to the microdomain volume, the overall crystallization rate increases by the same factor.

Notably, a two-step crystallization process was found 3 decades ago in an S/EO diblock ($w_{EO} = 0.30$) by Lotz and Kovacs[36] through dilatometry and subsequently confirmed by O'Malley et al.[43] by DSC on an essentially identical S/EO diblock. The two steps were of similar magnitude—but interestingly, those S/EO diblocks possessed a *cylindrical* morphology, not lamellar. As noted above, our cylinder-forming E/VCH diblocks (both E/VCH 6/25 and 10/26) crystallize in a *single* step, entirely by homogeneous nucleation. Also, Lotz and Kovacs noted the puzzling observation that the Avrami exponent for the lower-temperature process in their S/EO diblock was actually less than 1 ($n \approx 1/2$), rather than the simple first-order kinetics which we observe. The origin of these differences remains unclear.

Key aspects and parameters of crystallization for each of the E/VCH diblocks are summarized in Table 3. Often, the Avrami exponent n in eq 4 is considered to reflect the dimensionality of crystal growth, so one might anticipate different values for crystallization within spheres, cylinders, and lamellae. But we observe first-order kinetics whenever crystallization occurs within isolated microdomains, regardless of the microdomain dimensionality, because two essential conditions are satisfied. First, the extent of crystal growth is governed not by the impingement of crystals generated from neighboring nuclei but by the size of the microdomain itself. Second, E crystal growth throughout an entire microdomain is essentially instantaneous once nucleation occurs,[39] so the overall crystallization rate simply reflects the rate at which microdomains nucleate—which depends only on the *volume* of the crystallizable microdomains, not their shape.

Conclusions

Confinement within a block copolymer mesophase can radically alter polymer crystallization. At one extreme, subdividing the crystallizable material into nanoscale spheres requires the generation of one (homogeneous) nucleus per sphere to fully crystallize the specimen, and crystallization follows first-order kinetics. At the other extreme, highly interconnected structures such as the gyroid permit extended crystal growth from a single nucleus and exhibit sigmoidal crystallization kinetics resembling those of homopolymers. The impact of microdomain connectivity is particularly evident for lamellar materials; in an idealized lamellar structure, each lamella is isolated, but in real materials lamellae can be topologically connected through grain boundaries or other defects. Since the microdomains in the gyroid structure are more interconnected than are lamellar microdomains, the extent of microdomain connectivity is decidedly not a simple monotonic function (or even a unique function) of the volume fraction of crystallizable material in the block copolymer, but rather depends on the details of the connectivity at the scale of the grains. Though in the present case confinement was achieved with a glassy matrix block, we expect these findings to apply equally to the case where confinement is achieved through strong interblock segregation, provided confinement is complete.[44,45]

For the lamellar diblock studied here in detail (E/VCH 12/8), we found that approximately 85% of the E lamellae were isolated, requiring a homogeneous nucleus to be generated within each lamella to complete crystallization. We infer that the remaining 15% of the E lamellae are connected together into networks through which extended crystal growth is possible; for this fraction, crystallization is initiated heterogeneously, and the time for crystal growth through the network is comparable to the crystallization half-time, yielding sigmoidal crystallization kinetics. However, it is clear that these fractions are not universal, but rather must depend on the details of the grain boundary and defect structure within each lamellar material. Therefore, crystallization kinetics constitute a very sensitive probe of the connectivity between lamellae, as the “selectivity”—the ease with which a growing crystal can propagate within its own phase vs through the microdomains formed by the other block—is in principle boundless, limited only by the extent to which complete confinement can be achieved.

Acknowledgment. Financial support for this study came from the National Science Foundation, Polymers Program (DMR-9711436). The authors also thank EPSRC for Daresbury beamtime under Grant GR/M22116 to A.J.R. Y.-L.L. acknowledges the Princeton University Graduate School for the Porter Ogden Jacobus Fellowship.

References and Notes

(1) Hamley, I. W. *Adv. Polym. Sci.* **1999**, *148*, 113.
(2) Loo, Y.-L.; Register, R. A.; Ryan, A. J. *Phys. Rev. Lett.* **2000**, *84*, 4120.
(3) Quiram, D. J.; Register, R. A.; Marchand, G. R. *Macromolecules* **1997**, *30*, 4551.
(4) Rangarajan, P.; Register, R. A.; Fetters, L. J. *Macromolecules* **1993**, *26*, 4640.
(5) Rangarajan, P.; Register, R. A.; Fetters, L. J.; Bras, W.; Naylor, S.; Ryan, A. J. *Macromolecules* **1995**, *28*, 4932.
(6) Mai, S.-M.; Fairclough, J. P. A.; Viras, K.; Gorry, P. A.; Hamley, I. W.; Ryan, A. J.; Booth, C. *Macromolecules* **1997**, *30*, 8392.
(7) Quiram, D. J.; Register, R. A.; Marchand, G. R.; Adamson, D. H. *Macromolecules* **1998**, *31*, 4891.
(8) Weimann, P. A.; Hajduk, D. A.; Chu, C.; Chaffin, K. A.; Brodil, J. C.; Bates, F. S. *J. Polym. Sci., Part B: Polym. Phys.* **1999**, *37*, 2053.
(9) Loo, Y.-L.; Register, R. A.; Adamson, D. H. *Macromolecules* **2000**, *33*, 8361.
(10) Lotz, B. Ph.D. Thesis, Université de Strasbourg, 1963.
(11) Zhu, L.; Cheng, S. Z. D.; Calhoun, B. H.; Ge, Q.; Quirk, R. P.; Thomas, E. L.; Hsiao, B. S.; Yeh, F.-J.; Lotz, B. *J. Am. Chem. Soc.* **2000**, *122*, 5957.
(12) Zhu, L.; Cheng, S. Z. D.; Calhoun, B. H.; Ge, Q.; Quirk, R. P.; Thomas, E. L.; Hsiao, B. S.; Yeh, F.-J.; Lotz, B. *Polymer* **2001**, *42*, 5829.
(13) Cohen, R. E.; Cheng, P. L.; Douzinas, K.; Kofinas, P.; Berney, C. V. *Macromolecules* **1990**, *23*, 324.
(14) Hamley, I. W.; Fairclough, J. P. A.; Ryan, A. J.; Bates, F. S.; Towns-Andrews, E. *Polymer* **1996**, *37*, 4425.
(15) Hamley, I. W.; Fairclough, J. P. A.; Terrill, N. J.; Ryan, A. J.; Lipic, P. M.; Bates, F. S.; Towns-Andrews, E. *Macromolecules* **1996**, *29*, 8835.
(16) Loo, Y.-L.; Register, R. A.; Adamson, D. H. *J. Polym. Sci., Part B: Polym. Phys.* **2000**, *38*, 2564.
(17) Howard, P. R.; Crist, B. *J. Polym. Sci., Part B: Polym. Phys.* **1989**, *27*, 2269.
(18) Reichart, G. C. Ph.D. Thesis, Princeton University, 1997.
(19) Trent, J. S.; Scheinbeim, J. I.; Couchman, P. R. *Macromolecules* **1983**, *16*, 589.
(20) Lee, H. H.; Register, R. A.; Hajduk, D. A.; Gruner, S. M. *Polym. Eng. Sci.* **1996**, *25*, 6137.
(21) Register, R. A.; Bell, T. R. *J. Polym. Sci., Part B: Polym. Phys.* **1992**, *30*, 569.
(22) Adams, J. L.; Quiram, D. J.; Graessley, W. W.; Register, R. A.; Marchand, G. R. *Macromolecules* **1996**, *29*, 2929.
(23) Brandrup, J., Immergut, E. H., Eds.; *Polymer Handbook*, 3rd ed.; Wiley: New York, 1989.
(24) Walsh, D. J.; Graessley, W. W.; Datta, S.; Lohse, D. J.; Fetters, L. J. *Macromolecules* **1992**, *25*, 5236.
(25) Zoller, P.; Bolli, P.; Pahud, V.; Ackermann, H. *Rev. Sci. Instrum.* **1976**, *47*, 948.
(26) Rangarajan, P.; Register, R. A.; Adamson, D. H.; Fetters, L. J.; Bras, W.; Naylor, S.; Ryan, A. J. *Macromolecules* **1995**, *28*, 1422.
(27) Ryan, A. J.; Hamley, I. W.; Bras, W.; Bates, F. S. *Macromolecules* **1995**, *28*, 3860.
(28) Bras, W.; Derbyshire, G. E.; Devine, A.; Clark, S. M.; Cooke, J.; Komanschek, B. E.; Ryan, A. J. *J. Appl. Crystallogr.* **1995**, *28*, 26.
(29) Loo, Y.-L. Ph.D. Thesis, Princeton University, 2001.
(30) Hamley, I. W.; Fairclough, J. P. A.; Bates, F. S.; Ryan, A. J. *Polymer* **1998**, *39*, 1429.
(31) Sakurai, S.; Kawada, H.; Hashimoto, T.; Fetters, L. J. *Macromolecules* **1993**, *26*, 5796.
(32) Douzinas, K. C.; Cohen, R. E.; Halasa, A. F. *Macromolecules* **1991**, *24*, 4457.
(33) Avgeropoulos, A.; Dair, B. J.; Hadjichristidis, N.; Thomas, E. L. *Macromolecules* **1997**, *30*, 5634.
(34) Hajduk, D. A.; Harper, P. E.; Gruner, S. M.; Honeker, C. C.; Kim, G.; Thomas, E. L.; Fetters, L. J. *Macromolecules* **1994**, *27*, 4063.
(35) Bates, F. S.; Cohen, R. E.; Argon, A. S. *Macromolecules* **1983**, *16*, 1108.

(36) Lotz, B.; Kovacs, A. J. *Polym. Prepr. (Am. Chem. Soc., Div. Polym. Chem.)* **1969**, *10* (2), 820.

(37) Calculations were based on $\rho_{\mathrm{E,cryst}} = 0.986$ g/cm^3 (at 27 °C),[17] $\rho_{\mathrm{E,amorph}} = 0.856$ g/cm^3 (at 23 °C),[4] $\rho_{\mathrm{VCH}} = 0.950$ g/cm^3 (at 27 °C)[18] and $\alpha_{\mathrm{E,cryst}} = 3.0 \times 10^{-4}$/°C,[23] $\alpha_{\mathrm{E,amorph}} = 7.4 \times 10^{-4}$/°C,[46] and $\alpha_{\mathrm{VCH,glass}} = 2.2 \times 10^{-4}$/°C.[18]

(38) van der Sanden, M. C. M.; Meijer, H. E. H.; Lemstra, P. J. *Polymer* **1993**, *34*, 2148.

(39) Barham, P. J.; Jarvis, D. A.; Keller, A. *J. Polym. Sci., Polym. Phys. Ed.* **1982**, *20*, 1733.

(40) Koutsky, J. A.; Walton, A. G.; Baer, E. *J. Appl. Phys.* **1967**, *38*, 1832.

(41) Hong, S.; MacKnight, W. J.; Russell, T. P.; Gido, S. P. *Macromolecules* **2001**, *34*, 2398.

(42) Hong, S.; MacKnight, W. J.; Russell, T. P.; Gido, S. P. *Macromolecules* **2001**, *34*, 2876.

(43) O'Malley, J. J.; Crystal, R. G.; Erhardt, P. F. In *Block Polymers*; Aggrawal, S. L., Ed.; Plenum Press: New York, 1970.

(44) Loo, Y.-L.; Register, R. A.; Ryan, A. J., to be submitted to *Macromolecules*.

(45) Xu, J.-T.; Turner, S. C.; Fairclough, J. P. A.; Mai, S.-M.; Ryan, A. J.; Booth, C., submitted to *Macromolecules*.

(46) Graessley, W. W.; Krishnamoorti, R.; Balsara, N. P.; Butera, R. J.; Fetters, L. J.; Lohse, D. J.; Schulz, D. N.; Sissano, J. A. *Macromolecules* **1994**, *27*, 3896.

MA011521P